ADVANCED MATERIALS
www.advmat.de

Revisiting the "Stick-Slip" Process via Magnetism-Coupled Flexible Sensors with Bioinspired Ridge Architecture

*Dan Fang, Sen Ding, Yuhan Liu, Qian Zhou, Biao Qi, Bing Ji, and Bingpu Zhou**

"Stick-slip" phenomenon that occurs when human fingertip scans across a specific surface is essential to perceive the interactions between skin and the surface. Understanding the "stick-slip" behavior is important for bionic flexible system in applications from advanced robotics to intelligent tactile sensors. However, it is often overlooked owing to the limitations to mimic the soft skin that can tangentially deform/recover with informative electrical feedback. Here, a sandwich-type device with deformable ridge-layer is proposed to analyze the characteristic of stick/slip states in "stick-slip" process. Specifically, it is observed that fast recovery of the sensing architecture is caused by dynamic slip phase that generates periodical signals based on principle of induction. The results experimentally show that periods of the electrical pulses are dependent on factors such as inherent properties (e.g., modulus and geometry) and operational parameters (e.g., scanning speed and normal load), which is consistent with the theoretical model. Furthermore, it is found that the transition between "stick-slip" and full slip could qualitatively reflect interfacial properties such as moisture, roughness, and topology. It is expected that the results can strengthen the understanding of "stick-slip" behavior when fingertip interacts with a surface and provide guidance of flexible sensor design to enrich the biomimetic perceptions.

1. Introduction

The high-density distribution of tactile receptors beneath the fingertip skin enables rapid responses to external stimuli.[1] Various stimulus signals are transmitted through the nervous system to the brain, where they undergo comprehensive analysis to facilitate the perception of tactile information.[2] External stimuli primarily include normal pressure, tangential force, and relative sliding conditions.[3] Tactile perception encompasses information such as temperature, moisture, hardness, and roughness.[4] When in contact with an object's surface, fingertip skin undergoes deformation under the applied mechanical input.[5] This static contact process transmits certain physical properties to the brain. Apart from this, some physical surface features, e.g., roughness, require the determination through tangential relative motion between the fingertip skin and the target surface.[6]

Developing highly sensitive tactile bionic sensors is attracting abundant interest in research owing to the significant importance in promoting flexible electronics, health monitoring, artificial intelligence, and virtual reality technology.[7] Pressure sensors and slip sensors are two main categories of biomimetic tactile sensors. There have been sorts of flexible pressure sensors based on capacitive, resistive, and piezoelectric principles that can achieve high sensitivity detection over a wide linear pressure range.[8] Alternatively, current methodologies to detect sliding behavior are mostly based on analyzing the signal distribution of individual sensor units in the array to reflect the sliding state.[9] However, one main disadvantage of this method is that it requires a large number of electrode wires and signal transmission channels, which inevitably increases the complexity of wearable devices. In addition, collecting and analyzing signals from each channel is a complex process.[10] The range of relative sliding is limited by the size of the sensor array, and the sliding conditions outside the array range cannot be detected.[11] If a single sensor can follow the movement of an object, track and provide real-time

D. Fang, S. Ding, Y. Liu, B. Qi, B. Zhou
Joint Key Laboratory of the Ministry of Education
Institute of Applied Physics and Materials Engineering
University of Macau
Avenida da Universidade
Taipa, Macau 999078, China
E-mail: bpzhou@um.edu.mo

The ORCID identification number(s) for the author(s) of this article can be found under https://doi.org/10.1002/adma.202417867

DOI: 10.1002/adma.202417867

Q. Zhou
School of Physics
Central South University
Changsha 410083, China

B. Ji
School of Physics and Electronics
Hunan Normal University
Changsha 410081, China

B. Zhou
Department of Physics and Chemistry
Faculty of Science and Technology
University of Macau
Avenida da Universidade
Taipa, Macau 999078, China

feedback on the relative sliding condition, the problems existing in the sensor array might be addressed.

The interaction of frictional forces during relative motion between two contacted objects plays a critical role in perceiving slipping processes. According to friction theory, when these objects slide against each other, their mutual motion typically oscillates between static and sliding states due to dry friction's action known as stick-slip phenomenon.[12] During stick stage, static friction intensifies progressively and slippage will take place once the external force surpasses the maximum static friction force.[13] Previous studies have demonstrated that fingertip skin exhibits stick-slip behavior while gliding across specific surfaces, which renders repetitive stretching and recovery of the skin. Within this process, mechanoreceptors encode the dynamics as neural impulses in real-time and transmit related information to enable perception of such movements through neural system.[14] From this perspective, understanding the stick-slip process and clarifying involved factors are essential to further explore the function of biomimetic flexible sensors for electronic skins, advanced robotics and human–machine interactions. However, this branch is often overlooked in flexible sensors due to the limitations to mimic the soft skin that can tangentially deform/recover with informative electrical feedback. To date, it is still challenging to systematically analyze the stick-slip process through the application of individual flexible sensor.

To tackle this, we present a flexible tactile biomimetic sensor composed of a magnetized sandwich structure and copper coils for study of "stick-slip" phenomena. The top layer of the sandwich structure is a nonmagnetized polydimethylsiloxane (PDMS) layer primarily used for fixing the coils and the bottom layer is a magnetized flat film to interact with the target surface. The deformable layer, consisting of ridge-like structures, is capable to deform in tangential direction with recovery capability. Thanks to the magnetism-coupled approach, the rapid slip phase causes a fast change in magnetic flux within a short period, thereby generating current pulse signals in the coils via electromagnetic induction for behavior analysis. We first analyzed the detailed stick-slip process and studied the key factors that influence the stick/slip state. The results illustrate that both the inherent properties of the sensor and the operational parameters could influence the period of the slip pulses when the sensor scans across a specific surface. Regarding the period between two slip phases, the experimental results are in consistence with the established theoretical model. Second, we regulated the surface properties, e.g., moisture, roughness, to investigate the dependence of slipping or stationary processes on interfacial properties. It was concluded that the alternation of such information also effectively controls the occurrence of stick/slip process. Along with the demonstrated robustness, we expect that the methodology can provide a fresh understanding of stick/slip states in field of flexible sensors and prompt the sensor design toward the biomimetic functions especially for surface interaction.

2. Results and Discussion

2.1. Bioinspired Design Strategy

Perception of surface properties is one specific function of human fingertip. When a normal pressure is applied to fingertips for scanning across the surface of an object, the tactile receptors are capable to transmit information about the relative contact state between the skin and the surface to the brain through neurons. This information can be utilized to determine whether there is a stick or sliding status between the fingertip skin and the object surface, and the surface information, e.g., wetness, roughness, can thus be qualitatively perceived (**Figure 1a**). In principle, the skin of fingertip undergoes three typical stages during the above interactive process (Figure 1b). In stage A, the fingertip must apply specific pressure to ensure tight contact with the test surface, forming a defined contact area. As the fingertip then scans at a particular speed, in stage B, the skin tissue around contact area undergoes elastic deformation that generated stress (τ) in the skin. With further stretching, the skin stress is increased ($\tau' > \tau$), and finally reached the value of maximum static frictional force (f_{max}). At this point, the fingertip skin tends to recover from the stretched state to natural state (stage C) and contact transition from a stick state to a slip state occurs simultaneously. Due to the intrinsic elasticity of the skin, the sliding state during the recovery process is fast and the vibration process can be sensitively perceived by fast-adapting receptors to produce identifiable neural pulses. After recovery of the stretched skin, fingertip maintains contact with the object and continues to move forward. As the phenomenon of stick-slip periodically occurs from stages A to C, multiple pulse signals appear with a period T between adjacent pulse signals (Figure 1c), which can be decoded by the nervous system to analyze the interfacial information. However, if a specific surface is present, e.g., with lubricating medium on top, it is possible that only a pulse is generated at the moment of touch (Figure 1d). This stimuli difference would provide human the perceptive clue to identify the stick/slip states when interacting with a specific surface.

Various factors, such as the intrinsic skin properties, the operational parameters, and the interface condition, have been reported to play an important role that affects the perceptive function of fingertip during the stick-slip process.[15] Inspired by this phenomenon, it is essential that the sensing methodology requires a flexible device to maintain the tight connections among flexible components during the deformation processes. With this capability, the stick-slip process can be revisited with controllable parameters to investigate the parameter effects as human fingertip. Figure 1e shows our strategy, along with the biomimetic flexible device that is capable of lateral deformation and spontaneous recovery to revisit the stick-slip process when in contact with a specific surface. The flexible device consists of magnetized ridges that have been assembled and sealed between two facing substrates, and a flexible coil was integrated as an artificial neuron to detect mechanical deformation through identifiable electrical signals. When the intelligent finger is equipped with bionic device to scan across a specific surface, the elastic magnetized ridges can deform during stretching and rapidly recover when the static frictional force between the bottom substrate and target surface reaches its maximum value. According to Faraday's law of electromagnetic induction, rapid changes in magnetic flux can result in significant induced voltage peaks. Multiple repetitive processes may generate a series of voltage peaks that monitor the entire relative movement process during stick-slip transition. As shown in Figure 1f, the dimension of the flexible device is comparable to the human fingertip. With the sandwich-based

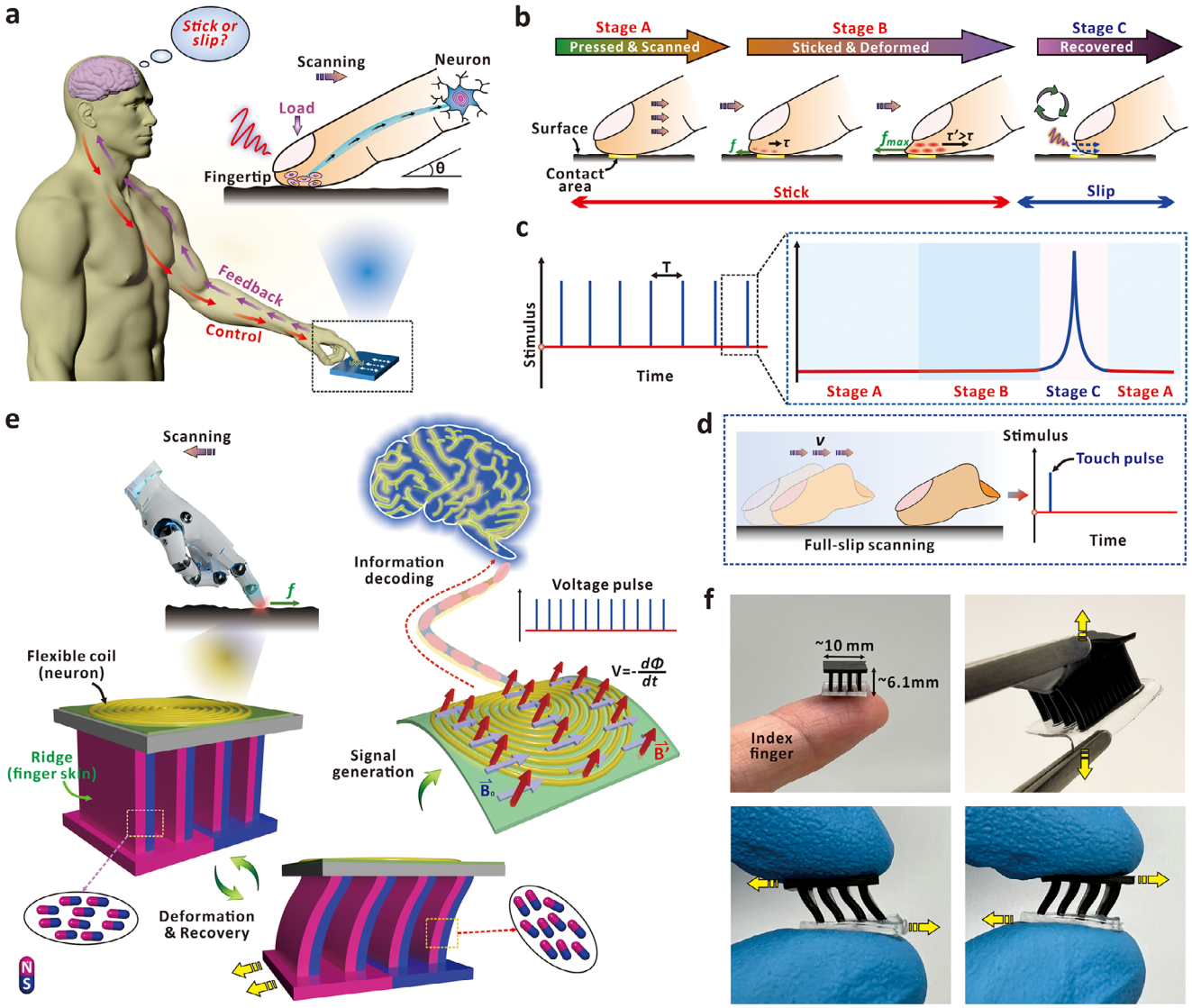

Figure 1. a) Illustration of the stick-slip sensing and feedback mechanism involving tactile neurons on the fingertip and the central nervous system. b) Three stages of deformation during one stick-slip cycle experienced by the skin when the fingertip scans across a specific surface. c) Schematic diagram of the bioelectrical pulses transmitted within the nervous system during the process described in (b). d) Schematic diagram of signals produced when the finger slides across a surface with full slip. e) Illustration of a sandwich-like magnetized device for stick-slip perception, featuring a deformable structure in the middle layer to mimic ridges on fingerprints with lateral deformation ability. The periodic deformation of devices will result in signal pulses for information decoding. f) Optical images of a typical flexible device when exposed to different kinds of mechanical deformation.

architecture, the assembly can withstand the stretch or lateral deformation with excellent recovery capability. We observed that the structure remained intact after separating the two substrates along both normal and tangential directions with gentle stretching. Energy-dispersive X-ray spectroscopy (EDS) and mapping presented in Figure S1 in the Supporting Information revealed the NdFeB permanent magnetized particles were uniformly dispersed within the soft matrix. Figure S2a in the Supporting Information provides the detailed design of the double-layer copper coils for signal collection. The optical images show that both line width and spacing between adjacent loops are ≈80 µm, with each layer containing ≈25 loops of the coils (Figure S2b, Supporting Information). Furthermore, there was no obvious resistance variation when the copper coil was bent or under natural status, ensuring the reliability of the flexible coil for signal collections during the characterization and wearable applications (Figure S2c, Supporting Information).

2.2. Overview of "Stick-Slip" Process

To precisely characterize the "stick-slip" behavior during the scanning process, we customized an experimental setup that consists of a normal force application system and a programmable motorized platform (**Figure 2**a). During the measurement, the flexible device was fixed on the indenter of a force gauge, which

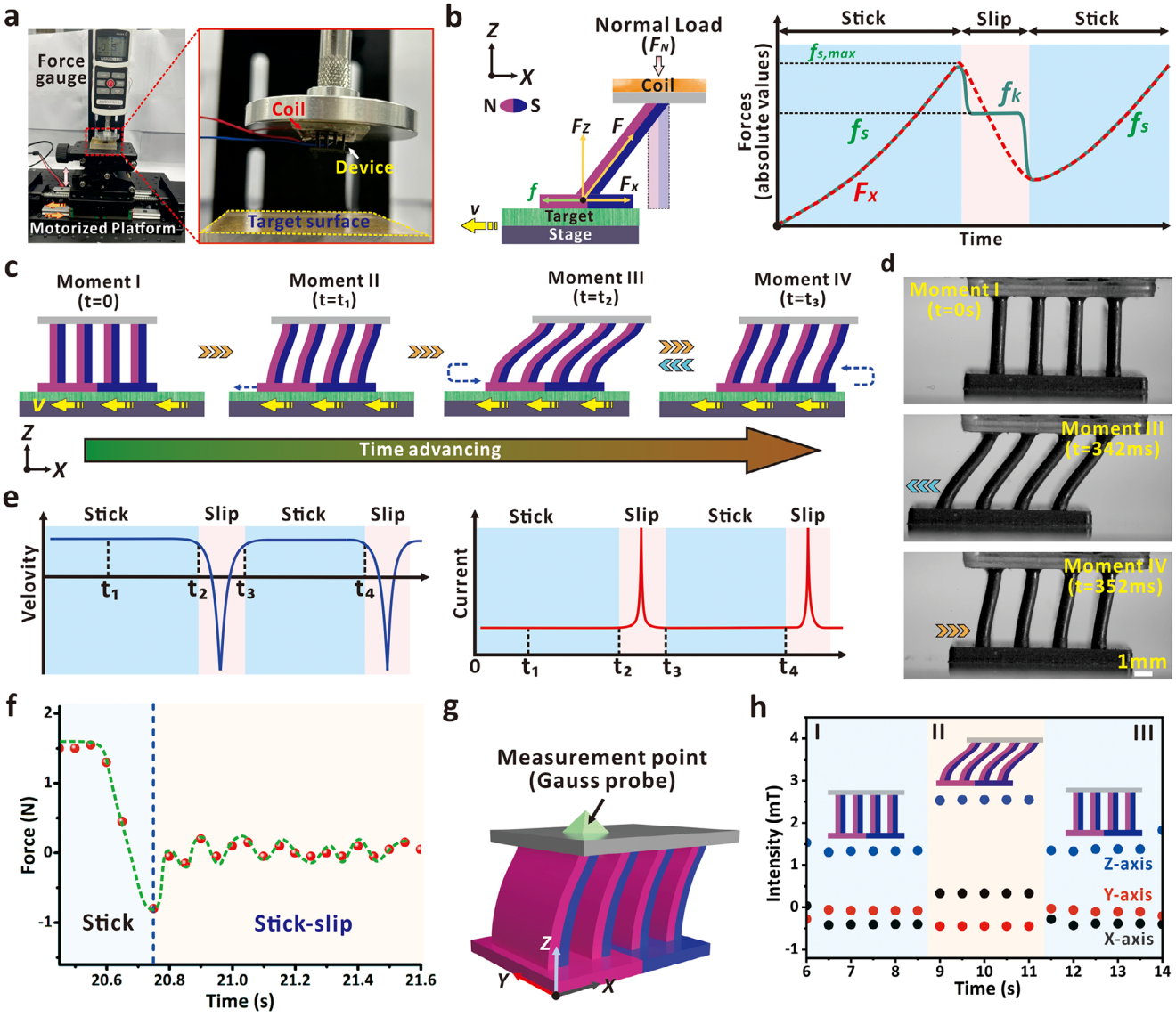

Figure 2. a) Optical images of the customized experimental setup for characterization of stick-slip behavior. b) Detailed force analysis on the flexible device during the stick-slip process. c) Schematic diagram of the morphological deformation during stick-slip process under different moments of stage. d) Real-time optical images showing the cross-sectional view of the device at I) initial, III) stretched, and IV) recovered status. e) Schematic representation of the variations in instantaneous velocity and induced currents during the periodical stick-slip process. f) Real-time monitoring of the normal load on top of the device during the motion of stick-slip process. g) Schematic diagram of measurements of localized magnetic field variation with a commercial gauss probe. h) Variation of the localized magnetic intensity in *X*, *Y*, and *Z* axes during the periodical motion of the device and platform.

was used to monitor the magnitude of the normal force applied on the flexible device. Via setting the vertical position of the motorized platform, the normal force could be adjusted to change the compression degree of the ridge layer. The motorized stage and target surface were externally controlled for precise back-and-forth motion with adjustable velocity/displacement for study. Involved forces acting on the specific ridges and the interface are further illustrated in Figure 2b, along with the morphological transformation in Figure 2c to describe a full "stick-slip" cycle. In principle, normal load (F_N), inherent elastic force (F), and frictional force (f) are primary influencing factors about the stick-slip behavior. As depicted in Figure 2c, a normal force (F_N) was applied to compress the flexible sensor against the test interface at moment I, $t = 0$. When the stage was moving laterally at constant velocity (v), the static frictional force guides the ridges of the device to deform laterally while the bottom substrate maintaining tight contact with the target interface. With time advancing, e.g., at time $t = t_1$, stick phase was preserved before the static frictional force (f_s) reaching the maximum value ($f_{s,max}$). In this period, the continuous motion would also lead to the changes in horizontal component (F_X) of the inherent elastic force (F). At a specific moment of $t = t_2$, the elastic strength is increased to reach the value of $f_{s,max}$, which leads to the instantaneous transition from static frictional force to kinetic friction (f_k) simultaneously. Note that the value of f_k is normally smaller than the value of $f_{s,max}$ at the moment of transition.[16] Even though the target surface

continues to move in $-X$ direction, the flexible device initiates a slip phase to recover in opposite direction ($+X$ axis). This is attributed by the significant drop from static to kinetic frictional force, and the inherent elastic force obviously exceeds the value of f_k. Compared with stick phase, the interval of slip phase is relatively shorter owing to the synergistic effect from the variation of inherent elastic strength and the kinetic friction. Upon completion of slip phase ($t = t_3$), the interfacial friction reverses the flexible device to move along the $-X$ direction as the stage for a new stick-slip cycle. Such process was recorded by high-speed camera, and the real-time optical images in Figure 2d indicates the bidirectional deformation of the ridges during the stick-slip process. As detailed in Video S1 in the Supporting Information, it can be observed that the slip phase requires an obviously shorter period (moment III to moment IV) when compared with the stick phase (moment I to moment III). As a result, a significant current signal can be induced to represent the slip phase for study of stick/slip status. We also noticed that the maximum stretching degree of the ridge during the first stick phase was relatively larger when compared with the subsequent stick-slip cycles (Video S1, Supporting Information). This is because from the second stick-slip cycles, the device was starting from slightly inclined status (Moment IV) instead of a vertical orientation (Moment I) due to the continuous movement of the stage. Consequently, the applied normal force is decomposed by the ridges to weaken the maximum static friction and the corresponding maximum stretching degree. As the first electrical pulse is generated after the first stick phase, this would not cause obvious deviation of the average period as discussed in the following section. The corresponding velocity and typical current profiles during the periodical stick-slip process are depicted in Figure 2e. During the stick phase, e.g., between t_1 and t_2, the bottom layer of the device moves along with the target surface. The relatively low moving velocity of the stage (stick phase) would not generate significant electrical pulse as presented in the current signal profile. The slip phase, starting from moment t_2, results in a rapid reversed velocity to produce a significant pulse because of the electromagnetic induction, which is also attributed by the reduced time to complete an equivalent amount of magnetic flux change. Similar as human fingertip, the series of periodical current pulses can serve as the informative clue to reflect the stick-slip process when the device scans across the target surface. We further monitored the real-time variation of normal load during the stick-slip process. As presented in Figure 2f, even though an initial normal load has been defined, it would continuously decay due to the stretch of the ridge layer in the stick period. Also, a slight fluctuation was periodically observed in the normal load when stick-slip occurs. This can be attributed by the repeated stretch and recovery of the ridge layer, which varies the compression degrees of the flexible device and thus the magnitude of the measured normal load. As demonstrated above, the kinetic friction can thus be considered as a constant function because the slip phase normally completes with a short period. Finally, a gauss probe was applied on top of the device to confirm the localized magnetic field variations in real-time during the periodical motions of the platform (Figure 2g). As the sampling rate of the gauss probe is relatively low when compared with the fast process of "stick-slip", we alternatively preserved the deformed status of the ridge layer to monitor the magnetic field variation. For example, after the displacement of the platform and the deformation of the device, the magnetic field intensity along X, Y, and Z axes varies significantly as shown from region I to region II in Figure 2h. The magnetic field distribution remained unchanged if under the preserved deformed status, and returned to the initial values once the device recovered to the original status (from region II to region III). The results confirm that the localized magnetic field can be tuned because of the repeated stretch and recovery of the magnetized ridges. With such built-in magnetized orientation, the ridge-based architecture would allow the stick-slip process to be characterized by the electrical signals based on electromagnetic induction.

2.3. Dependence of "Stick-Slip" on Inherent Properties

It is evident that the inherent characteristics of the device play an important role to influence the elastic properties of the magnetized ridges, which would potentially affect the signal profiles during the periodical "stick-slip" process. To confirm this, we investigated how the dimensional parameters and shear modulus would guide the signals during the scanning process. As depicted in **Figure 3**a, width (W), depth (D), and height (H) are three crucial physical parameters of the stripe-like ridges, especially W and H can significantly affect the capability of lateral deformation along X direction. Herein, the value of D was fixed at 8 mm because the scanning process is mainly directed along X-axis. We simplified the ridge structure to a spring model to examine the effects of the forces involved during the stick-slip process (Figure 3b). The ridges, as deformable layer, are subjected to the inherent force that is related with the deformation degree and elastic coefficient of the PDMS/Ecoflex matrix. Consequently, the synergistic effect from kinetic friction (f_k) and restoring force renders the slip phase as an ideal harmonic motion. From this perspective, the interval of periodical pulse is one essential property of the stick-slip process, which mimics the periodical signals in neural system to reflect the stick/slip states as human fingertip. Through theoretical analysis (Note S1, Supporting Information), we found that the period (T) of two adjacent peaks from the stick-slip process could be denoted as

$$T = \frac{f_{s,max} - \mu_k F_N}{v_s \cdot k} \tag{1}$$

where $f_{s,max}$ is the maximum static frictional force, μ_k is the kinetic frictional coefficient, F_N is the normal load, v_s is the scanning speed, and k is the equivalent elastic coefficient of the ridges. Basically, the formula incorporates the main factors that determine the interval between two adjacent "stick-slip" cycles. We first examined the influence from the equivalent elastic coefficient (k) based on the customized system and standard evaluation setup as shown in Figure S3 in the Supporting Information. To ensure the shielding effect from environment, we initially monitored the electrical signals from the coils when the motorized platform was periodically moving along $+X/-X$ directions. As shown in Figure S4 in the Supporting Information, only weak noise signals were collected, confirming that the magnetic field in the surroundings would not

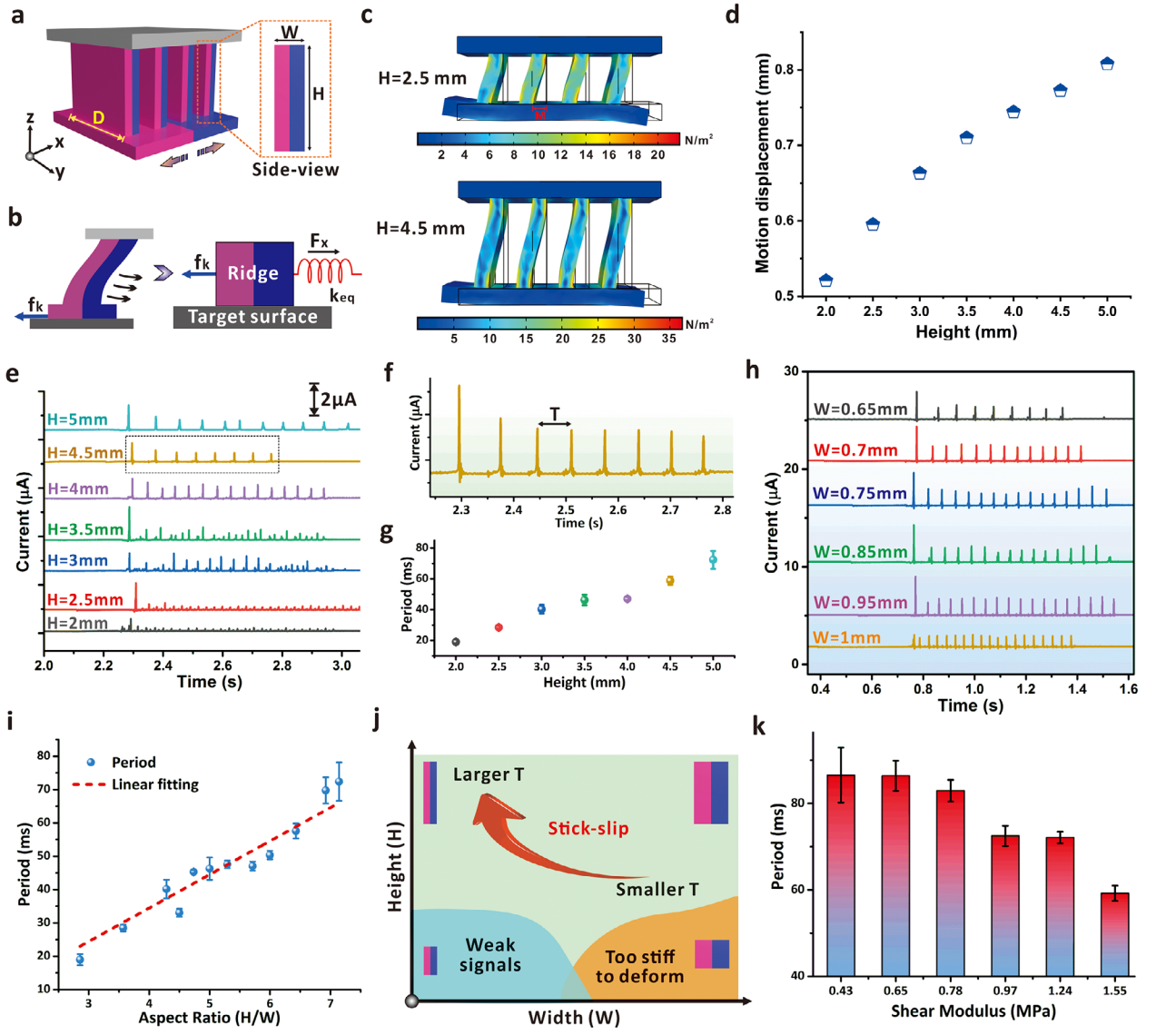

Figure 3. a) Schematic diagram of the primary volume parameters of the ridges in the ridge layer, including depth (*D*), height (*H*), and width (*W*). b) Schematic diagram of force analysis for a single ridge along the movement direction of the target surface. c) Transient static simulation results of the force distribution under maximum deformation when subjected to a 1 N normal load and 0.38 N tangential frictional force. The motion displacement (*M*) refers to the maximum distance moved by a reference point in the lateral direction. The heights of the ridges are 2.5 mm (top) and 4.5 mm (bottom) in the simulation model. d) Summary of motion displacement based on the simulation results from devices with varying ridge heights. e) Current profiles during stick-slip processes generated by flexible devices with different ridge heights. f) Amplified signals with ridge height of 4.5 mm. "*T*" denotes the time interval between two adjacent slip processes. g) Variation of average pulse periods by changing the ridge heights of the flexible device. h) Current profiles collected by coils when the ridge widths of the device were changed. The ridge height is constant as 4.5 mm. i) Linear fitting results of the relationship between pulse period and the aspect ratio of the ridge. The obtained function is $y = 10.04x - 4.71$ with R^2 of 0.8508. j) Illustration of the dependence of stick-slip formation and signal period (*T*) on the height and width of the ridge layer. k) Variation of pulse periods based on the flexible devices prepared by the composites with different shear moduli.

interfere with the experimental results during the "stick-slip" process. Furthermore, Figure S5 in the Supporting Information compares the signal profiles when the devices were prepared with or without a magnetized top layer that was attached to the coil side. No obvious deviation of signal periods was observed, indicating that the immobilized layer would not affect the behavior of stick-slip process. For better differentiation, we utilized pure PDMS to serve as the immobilized layer for following studies.

In principle, the *k* value is linearly proportional to the ratio of the ridge width and height ($k \propto \frac{W}{H}$) as well as the shear modulus (*G*). Similar with the stretching and recovery of fingertip skin, lateral deformation of the ridges in the flexible device plays an important role to provide electrical feedback of the surface property.[17] Prior to the systematical evaluation, we thus prepared the flexible devices with different shapes of deformable layer to compare the deformation capability. As shown in Figure S6 in the Supporting Information, three types, including

cuboid array, cylinder array, and ridge array, have been designed as the deformable layer for the sandwich-type device. For parallel comparison, all deformable layers were designed to contain an equal volume of magnetized components. To compare the deformability of different arrays, we first used COMSOL Multiphysics to simulate the force distributions under the same force condition. In Figure S7 in the Supporting Information, it is evident that the load-bearing area of cylinder-shaped deformable layer is smaller than the other two types (cuboid and ridge arrays). The electrical profile further illustrates that no stick-slip phenomenon occurs in the cylinder-shaped flexible device due to the limited stretch and recovery capability along the deformation direction (Figure S8a, Supporting Information). For cuboid and ridge layers, the flexible device could render successful stick-slip process with periodical signals thanks to the capability of lateral deformation (Figure S8b, Supporting Information). Considering the lateral deformation is mainly in one dimension (e.g., *X*-axis), we adopted the ridge-type as deformable layer for the flexible device in subsequent studies. Note that the volume of magnetized ridges is also essential to provide magnetic flux variation during the stick-slip process. From this perspective, we prepared the device with different ridge numbers from 2 to 6 as shown in the optical images in Figure S9a in the Supporting Information. For parallel comparison, the total area of each device was kept identical. Based on the standard characterization, it can be observed that the pulse intensity obviously increases when the ridge number was changed from 2 to 4 (Figure S9b, Supporting Information), which might be attributed by more involved amount of magnetized components. With further increased ridge number to 5 or 6, the electrical signals also exhibit slightly enhanced behavior. Taking both the fabrication methodology (e.g., efficiency of mold production) and signal intensities into consideration, we finally fixed the ridge number at four for the following investigations as it could provide accessible electrical signals for analysis.

Followed with this, we simulated the deformation capability of ridges with varying heights. As presented in Figure 3c and Figure S10 in the Supporting Information, the lateral deformation of the ridge layer was ensured when a normal load and horizontal friction were applied. We applied "M" to denote the motion displacement in the simulation, and Figure 3d provides the value of displacement that is dependent on the height of the ridge. In general, a higher ridge would result in a larger motion displacement due to the higher degree of deformation if the width of the ridge remains the same. Based on above, the flexible sensor with ridge-type deformable layer was applied to investigate the "stick-slip" process when scanning across an acrylic surface. Figure 3e records the electrical signals when the heights of the ridges were changed from 2 to 5 mm. The results reveal that more significant pulses can be regularly produced if the device is prepared with a higher ridge (see Figure S11, Supporting Information, for the flexible devices with different ridge heights). However, it is difficult to obtain a clear picture that describes the dependence of peak magnitudes on the ridge heights. This suggests that the perception of stick/slip state is closely related with signal frequency instead of the magnitude scale.[18] We also observe that a higher ridge can normally produce stronger pulses during the rapid recovery of the slip process. This can be attributed by the higher quantities of magnetized components and thus a more obvious magnetic flux variation during the motion. Figure 3f further provides an enlarged view of the signals produced from the device with ridge height of 4.5 mm. Here, "*T*" represents the time interval between two adjacent peaks, signifying the oscillation period between consecutive electrical peaks. As summarized in Figure 3g, the average values of "*T*" are positively correlated with the height of the ridge. A higher ridge would normally result in enhanced flexibility that prolongs the time to reach maximum stretching during the stick phase, which corresponds with the theoretical model as demonstrated above. Furthermore, we fixed the height of the ridge as 4.5 mm and altered the width to evaluate the impact on signal profiles during the periodical "stick-slip" processes. Figure S12 in the Supporting Information shows the optical images of different devices with ridge width from 0.65 to 1 mm, and the corresponding current profiles were displayed in Figure 3h. With a larger ridge width, the values of period continuously decrease, indicating a shorter duration of the stick phase because of the less time to reach the maximum stretching status (Figure S13, Supporting Information). Combining the height and width, we summarized the dependence of period on the aspect ratio (H/W). As shown in Figure 3i, the fitting results indicate the linear relationship between the "stick-slip" period and the aspect ratio, which further confirms the effect from the equivalent elastic coefficient ($T \propto \frac{1}{k}$). The schematic diagram in Figure 3j summarizes the selection of dimensional parameters for possible "stick-slip" formation. Generally, excessive ridge width would result in the difficulty of lateral deformation and recovery, whereas shorter ridges are not reliable to generate intensive signals due to the limited magnetized volumes. With appropriate design of aspect ratio, periodical pulses can be ensured according to the "stick-slip" process, and a larger value of aspect ratio is related with a slower stick phase (larger *T*) if the interfacial property remains unchanged. Similar as aging of human skin, mechanical property of the device is another parameter that might impose influence to the tactile perception and generation of electrical signals.[19] Apart from the aspect ratio, we thus regulated the intrinsic shear modulus of the matrix to evaluate the deformation capability and thus the "stick-slip" behavior. Based on different mass ratios of Ecoflex and PDMS, the shear moduli were obtained from the measured elastic modulus (Figure S14, Supporting Information) and Poisson's ratio (Table S1, Supporting Information). With a fixed width (0.7 mm) and height (4.5 mm) of the ridge layer, the devices prepared with different shear moduli also exhibit significant "stick-slip" behavior as presented by the electrical signals in Figure S15 in the Supporting Information. Based on the theoretical model, the ridge's modulus or equivalent elastic coefficient (k) is essential to determine the device ability of lateral deformation. A larger value of modulus would lead to decreased deformation capability during the stick-slip process. Consequently, the devices prepared by materials with a higher degree of modulus result in a smaller slip length. Under the same scanning speed, a shorter interval between adjacent pulses of two slip phases will then be observed. As presented in Figure 3k, a smaller period was obtained from the electrical signals when the device was prepared by the composite with higher shear modulus. However, the limited range of shear modulus obtained by adjusting the ratio of PDMS and Ecoflex does not allow the pulse period to exhibit an obvious inversely proportional trend as predicted in the theoretical model.

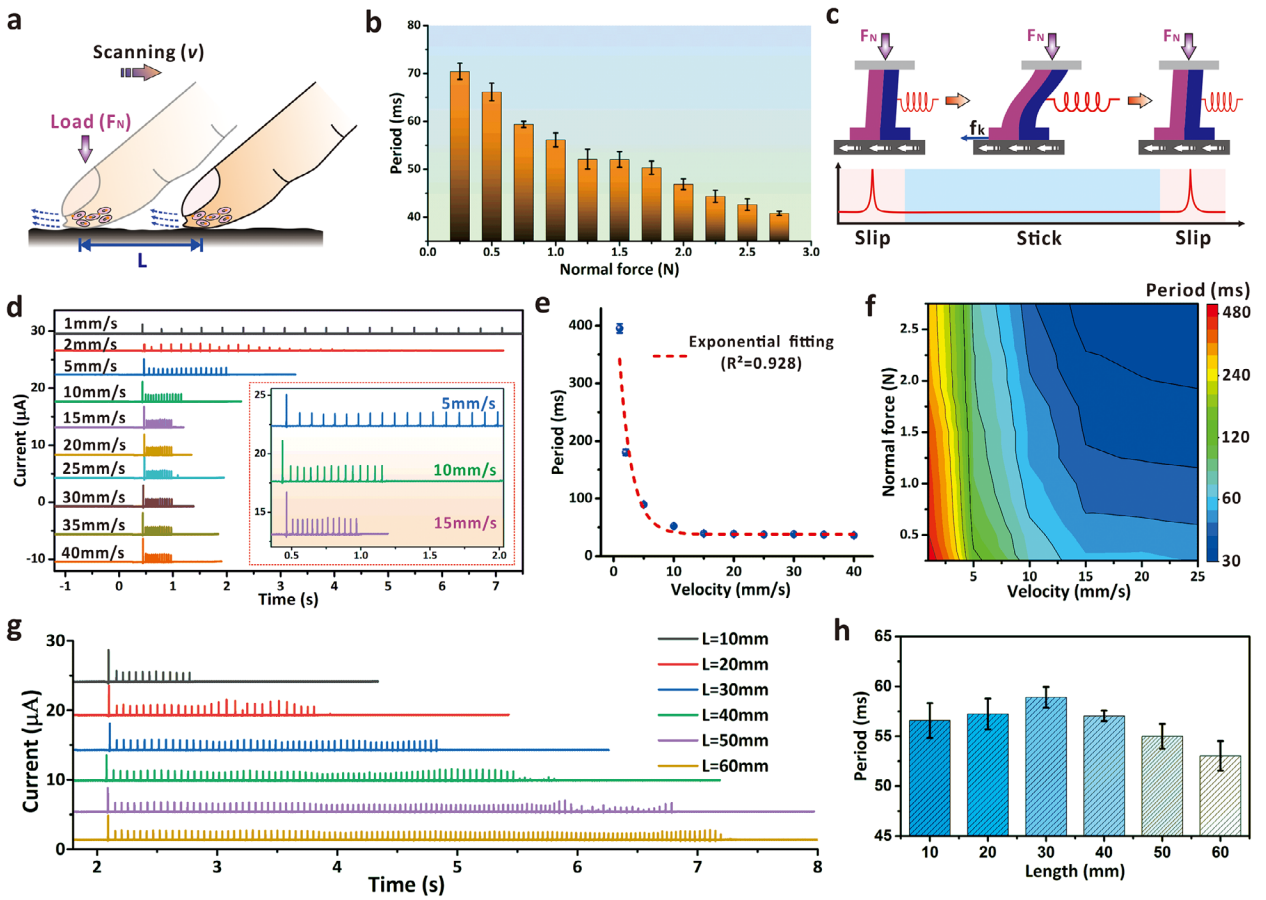

Figure 4. a) Illustration of the crucial external parameters, scanning velocity (v), normal load (F_N), and scanning distance (L), that may affect the generation of biosignals when a finger scans across a surface. b) The periods of electrical pulses during the stick-slip process when different normal loads were applied to the device for evaluation. c) Schematic diagram of variation in elastic force during the ridge deformation in one stick-slip cycle. The length of the spring is positively correlated with the elastic force, and the frictional force is related with the applied normal force F_N. d) Current profiles generated by the same device under different scanning speeds. e) Exponential fitting results of pulse period and applied scanning velocity ($R^2 = 0.928$). f) Summary of periods generated by a device under varying scanning velocities and normal loads. g) Current profiles generated at different scanning distances by the device with $H = 4.5$ mm and $W = 0.7$ mm. The scanning speed is 10 mm s^{-1} and F_N is 1.5 N. h) Average period of the slip peaks based on different scanning distances.

Based on the current composite matrix, the shear modulus was regulated within the range of 0.43–1.55 MPa. It can be expected that the experimental results can reveal a higher degree of consistence with the governing formula if a composite matrix with wider modulus range can be achieved.[20]

2.4. Operational Parameters Govern Stick-Slip Behavior

In addition to the inherent properties of flexible device, the behavior of stick-slip process is possibly influenced by manual operations during finger scanning (**Figure** 4a). In view of this, we conducted a comprehensive investigation into the relationship between electrical signals and external stimuli, such as loading force (F_N), scanning speed (v) and length (L). For this study, we employed a typical device with $G = 1.55$ MPa, $W = 0.7$ mm, and $H = 4.5$ mm for the ridge layer (aspect ratio of 6). Figure S16 in the Supporting Information records the electrical profiles obtained under different normal forces, revealing that the period between two adjacent slip phases decreases when the normal force is increasing (Figure 4b). This phenomenon can be explained by the force analysis model in Figure 4c, which describes the force variation between two adjacent slip phases. For our experiments, restoring force from the ridge layer is dependent on the deformation degree. In our case of applying different values of normal force, a larger F_N would limit the maximum displacement of the ridge-layer, resulting in a reduced time to complete the stick phase when scanning speed was unchanged. It also can be observed that the values of normal force will not obviously affect the amplitude of the current pulses (Figure S16a, Supporting Information). As discussed above, the period of adjacent pulses is mainly determined by the interval between two slip phases. However, according to Faraday's law of induction, the pulse amplitude is mainly affected by two factors, namely the change of magnetic flux in the conductive loop and the corresponding duration. The enlarged signal profiles in Figure S16b in the Supporting Information show that the duration for each pulse is 3–5 ms when different normal forces were

applied. This is consistent with the rapid slip status. Furthermore, the optical images indicate that the difference in compression degree is negligible when normal forces of 0.25 and 2.75 N were applied to the device (Figure S17, Supporting Information). This would result in insignificant difference in change of the magnetic flux during the lateral deformation and recovery process. Consequently, the amplitude of the current signal is almost unaffected by the negligible differences in these two parameters. From this perspective, the signal period plays an essential role to reflect the behavior of the "stick-slip" process instead of the signal intensities. Moreover, it is also important to note that an excessive normal force would impose significant normal deformation of the complete device, which will bring difficulty to the ridge layer for lateral deformation during the stick-slip process. As shown in Figure S17 in the Supporting Information, irregular lateral deformation occurs at each ridge when the normal force exceeds 6 N. This might finally result in a notable increase of period or even disappearance of periodical pulses because of the prolonged stick phase. Under the same condition, we further examined the minimum normal load that can be applied to produce electrical signals during the stick-slip process. Figure S18 in the Supporting Information presents that the periodical pulses could not be stably produced if a decreased normal load of 7 mN was applied to the device. The results experimentally suggest that a sufficient normal force to ensure the tight interaction between the device and a surface is required for successful stick-slip behavior, which indicates that the normal load and frictional force are important to regulate the stick phase as described in the theoretical model.

We further elaborate on the scanning speed and analyze the corresponding period to determine the underlying relationship. By regulating the speed of motorized platform, the target surface was forced to move along *x*-axis under different speeds from 1 to 40 mm s^{-1} (Figure S19, Supporting Information). In Figure 4d, we observe that the total duration of the stick-slip process varies with the applied moving speed when the covered distance (L) remained unchanged. Specifically, the enlarged electrical profiles display the obvious difference in period of the slip peaks, where a longer period is normally related with a smaller moving velocity of the platform. Furthermore, the fitting results of experimental periods represent an exponential relationship with the motion speed (Figure 4e), which is consistent with the theoretical derivation in Note S1 in the Supporting Information. When the scanning speed exceeds 10 mm s^{-1}, difference in periods decreases as the required time to complete one full stick-slip cycle is obviously reduced at this range of speeds. Based on above, the synergistic effect from normal force and scanning velocity on the period is summarized in Figure 4f. The mapping results indicate that upon the existence of stick-slip behavior, selective combinations of scanning speed (1–25 mm s^{-1}) and normal load (0.25–2.75 N) would produce regular current pluses with specific period. It is conceivable that both lower scanning velocity and smaller normal force facilitates the differentiation of periods even with the same interfacial property. With a faster scanning velocity and large normal force, the period will be shortened as the time required to change the status from "slip" to maximum "stick" is significantly reduced under such conditions. We further evaluated the effect of scanning length, L, on the signal profile (see Figure S20, Supporting Information, for evaluation setup and period distribution). In principle, the change of scanning length will result in varying number of signal pulses. However, the average period should remain in a relatively stable range due to the unchanged conditions such as normal force, scanning speed or interfacial property. As shown in Figure 4g, the number of induced pulses increases with moving distance due to the occurrence of stick-slip process in continuous relative motion. Furthermore, the signal period does not significantly change with moving distance, indicating the consistency with our hypothesis that the period of stick-slip process is independent of travel distance (Figure 4h). Even though fluctuation occurs in the period when different scanning lengths were applied, however, this cannot be summarized as length-dependent phenomenon by principle. Note that the signal fluctuation at the end of the signal spectra is mainly caused by the deceleration process of the motorized platform. This fluctuation would not affect the resultant period because the value is normally obtained from the typical peaks when the platform was moving under a relatively stable status. We further carried out parallel experiments to examine the signal reliability under different scanning lengths (Figure S21, Supporting Information). It can be observed that signal attenuation was existent in the spectra, however, the main peaks for period acquisition remain almost unaffected as presented in the enlarged profiles.

2.5. Reliability and Robustness of Ridge-Type Sensors

For real applications, the stability of the developed flexible device should be assessed to determine its reliability owing to the repeated mechanical stretching and release. To confirm this, the platform was controlled to move across the flexible device back-and-forth for ten identical cycles. The induced signals were presented in **Figure 5**a, which reveals that periodical "stick-slip" processes occur in both scanning directions. We also observe that periodic signal pulses can be stably produced, and the related period values for each cycle in both directions were provided in Figure 5b. The difference between average periods from $-X$ and $+X$ directions is less than 10 ms, indicating the reliability of the flexible sensors in both lateral deformations. Furthermore, consistent signals were obtained from the device after 2000 cycles' fatigue test of lateral stretching and recovery (Figure S22, Supporting Information). As shown in the optical images (Figure S22a, Supporting Information), no obvious cracks were observed in the sandwich-type architecture of the device, suggesting the mechanical stability after periodical deformation in lateral direction. We could observe that periodical signal peaks were stably obtained, which indicates the successful ridge deformation and recovery during the stability test (Figure S22b, Supporting Information). The average period in Figure S22d in the Supporting Information shows the consistence of the device performance between the initial state and after the fatigue test. The results illustrate that the flexible device is capable to withstand long-term lateral stretching and perceive the stick/slip status through repeatable electrical signals when contacting with a specific surface.

In our experiment, we fixed the position of the coil and device assembly, while simultaneously controlling the target on the motorized platform to enable a relative motion between the two components. One may concern that this situation is contrary to the behavior when human finger scans across a target surface.

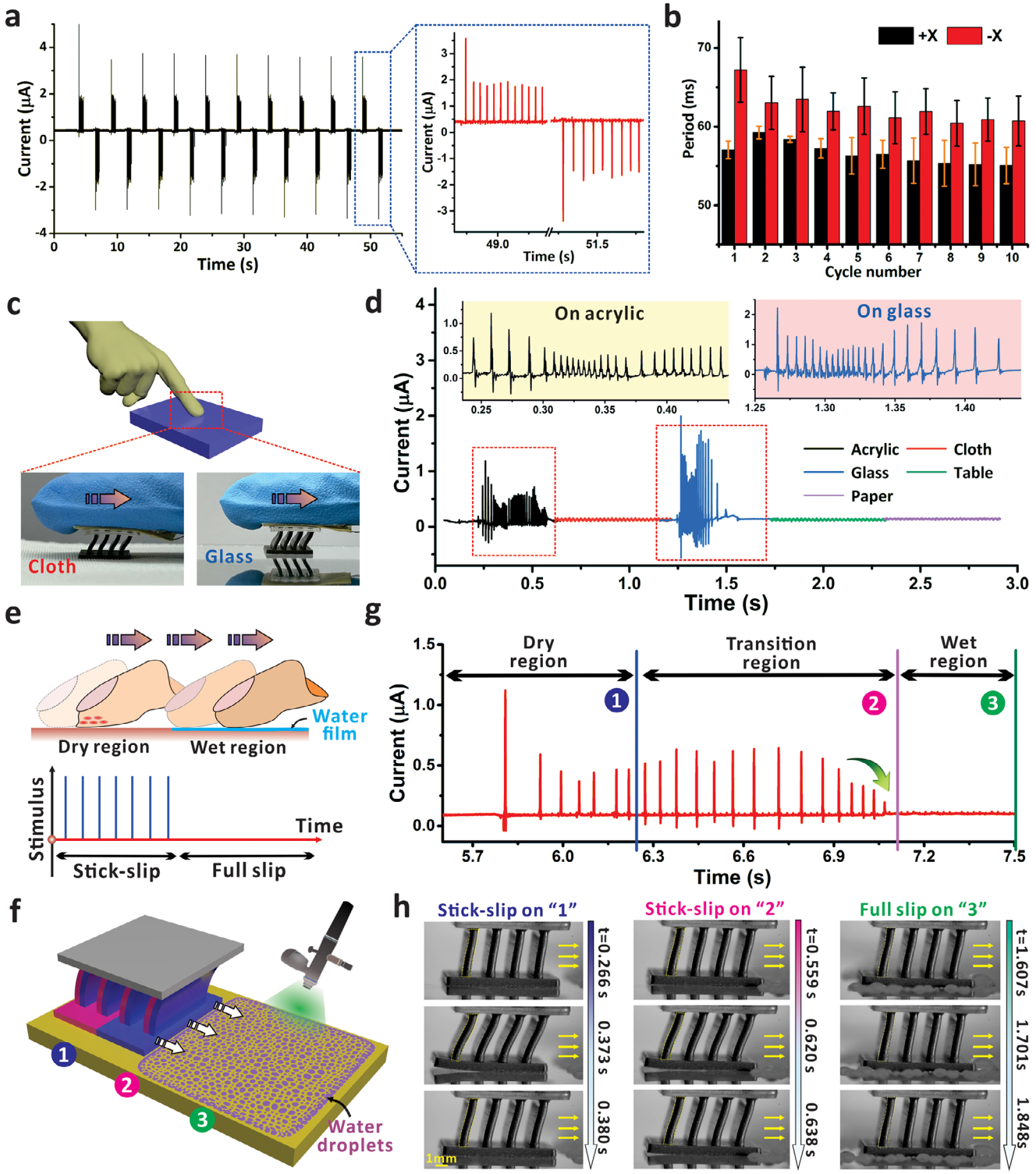

Figure 5. a) Electrical profiles when the device moves across a target surface for ten cycles. Positive peaks were generated when moving in *+X* direction, while negative peaks were produced in *−X* direction. b) Average periods obtained from each peak group in (a). c) Schematic diagram of finger scanning across a specific surface, and the optical images show the flexible device was attached on the fingertip to scan across cloth and glass substrates. d) Electrical signals when the device was attached on human fingertip to scan across different substrates. The enlarged profiles are related with acrylic and glass surface. e) Schematic diagram of the finger scanning from dry to wet regions with related signal production. f) Setup of scanning across the surface with different wetting properties. "1" is dry region, "3" is the wet region, and "2" is the transition region between them. g) Current profiles when the flexible device scans from dry to wet regions of the same acrylic substrate. h) Optical images of the flexible device when scanning across the surface at locations 1, 2, and 3 with different behaviors.

Normally, participant moves the fingertip across a static surface to perceive the surface property of the target. To investigate whether the difference in setup configuration would affect the signal profiles, we alternatively fixed the target surface and changed the device position to study the process (Figure S23a, Supporting Information). During the moving of the platform, periodical ridge stretch and recovery were also observed, exhibiting a typical stick-slip behavior. As shown in Figure S23 in the Supporting Information, there was no significant difference in the profile and the periods between adjacent slip phases remained almost unaffected. The results validate the design of our customized setup, and further confirm the importance of the ridge-based architecture for generation of periodical signals. Furthermore, we attached the flexible device on finger pad and scan across the surface to mimic the perceptive function of human finger and evaluate the potential toward real tactile applications (see Video S2, Supporting Information, for real-time record). The optical images show the setup to manually scan across different surfaces, e.g., cloth and glass, via attaching the sensor on the index finger (Figure 5c). When scanning across different substrates, we monitored the induced electrical signals from the wearable sensor to reflect the "stick-slip" or "full slip" phenomenon (Figure 5d). A full slip behavior was observed on the relatively rough surface, e.g., cloth, table, and paper. Enlarged electrical profiles were provided alongside, which indicates the periodical pulses that can be related with the slip phase during the manual operation. The results indicate that the stick-slip process occurs on solid and smooth materials such as acrylic plate and glass, but is absent from substrates such as paper, cloth, and tables. Note that the deviation of periods is attributed by the speed fluctuation during the manual scanning, which can be further confirmed by the detailed electrical profiles in Figure S24 in the Supporting Information. The results validate the function of our wearable device, which successfully mimic the capability of human fingertip to revisit the stick/slip status when scanning across a surface.

2.6. Influence of Surface Moisture on Stick/Slip States

Surface moisture, or wetness, is one interfacial parameter that appears to affect the psychophysical perception of stick-slip process during finger scanning.[21] As presented in Figure 5e, when the fingertip scans from the dry to wet region that has been wetted by water film, full slip can possibly occur because of the insufficient skin stretch and the insignificant difference between static and kinetic frictional forces.[22] However, such case of signal transition is difficult to be fully reproduced using conventional flexible sensors. Based on our developed sensor, we demonstrated a direct approach to explore the moisture effect on stick/slip state perception by manually regulating the water content on the acrylic substrate. We utilized a spray gun to partially wet the acrylic surface, and allowed the flexible device to scan across the surface from nonwetted to wetted region for signal comparison (Figure 5f). The current signals in Figure 5g exhibit an obvious difference when the device was scanning across the acrylic surface. In the dry region, the stick-slip process led to periodical impulses, which are related with the rapid "slip" phase according to Faraday's law of induction. We also observed that the device experienced "stick-slip" process when moving across the dry to wet region (②). This is reasonable before the bottom of the flexible device was fully wetted by the water film, which can be further confirmed in Video S3 in the Supporting Information. Without sufficient stretch caused by target surface, the "stick-slip" cannot be supported, and periodical impulse will finally vanish after crossing the dry region. The optical images in Figure 5h further confirm the different behaviors of ridge deformation across the indicated regions. For region ③, it is evident that a full slip process was existent, and the total device could maintain a stable stretched status to cross the wet region. However, obvious stick-slip process was observed on regions ① and ②, which shows the stretch and recovery of the ridges during the motion process. As discussed above, such existence of the water film could weaken the contact between two surfaces. Consequently, the attenuation of frictional force further reduces the difference between static and kinetic frictions which is required for a successful stick-slip process. This is consistent with the model that the variation between static and kinetic frictional forces is important to support the stick-slip behavior for perception. The results support that surface moisture is one critical parameter that affects the nervous perception of stick/slip state when fingertip is scanning across a surface. From this perspective, the wearable sensors with immune capability to humid environment are preferred to precisely reflect the processes of stick-slip or full slip.[23]

Furthermore, we controlled the surface moisture by adjusting the spraying time to evaluate the detailed impact from interfacial wetness. As presented in Figure S25 in the Supporting Information, accumulation of water droplets on the acrylic plate was manually controlled by increasing the spraying duration from 1 to 20 s. With obvious droplet deposition on surface, stick-slip phenomenon quickly vanished and only a slip pulse occurred when ridge stretching converted to the kinetic mode (Figure S26, Supporting Information). With the presence of a water film, the frictional force significantly decreased because of the well-known lubricating effect.[24] Consequently, the sticking behavior was unable to be supported, and continuous slipping of the device on the surface was observed without periodical pulse signals. Video S4 in the Supporting Information recorded the real-time process when the device was moving across a wetted acrylic surface, and "stick" to "slip" transition was clearly accompanied with a significant electrical pulse (Figure S27, Supporting Information). After the embryonic stick-slip process, full slip behavior was stably maintained without periodical ridge deformation and recovery as shown in the real-time captures. The results experimentally indicate that surface moisture is essential for the stick-slip or full slip situation, which is responsible for signal generation that plays an important role to influence the human perception when interacting with the surface.

2.7. Roughness-Oriented Stick-Slip/Full Slip Behavior

The analysis above has confirmed the essential role of intrinsic properties and operation parameters to determine the interactive behavior during the scanning process. When human fingertip slides across a specific surface, the perception of stick-slip process is also affected by the interfacial property, e.g., roughness or morphology.[25] Considering this, investigating the influence

from target surface helps to further clarify the stick-slip behavior, which is significant for optimization of the sensing capability toward biomimetics. We firstly selected nine typical examples including steel, Aluminum (Al), glass, PDMS, and paper, etc., to examine the effect from different surfaces (see Table S2, Supporting Information, for related coefficient of friction). The corresponding electrical signals were recorded in **Figure 6**a, which shows periodical current pulses due to the occurrence of "stick-slip" except the paper and sandpaper substrates. Furthermore, we found that the intervals of periodical pulses from different profiles commonly located in range of 60 ± 10 ms (Figure S28, Supporting Information). Upon tight contact between the device and the target surface, the similar intrinsic coefficients of friction of these smooth materials play an important factor to obtain approximate periods of pulse from the current spectra. The results indicate that under the same operations, the flexible device is capable to electrically identify the stick or slip state when crossing the target surface. As recorded in Video S5 in the Supporting Information, a full slip process was clearly demonstrated when the device was scanning across the paper surface with slight incline. Even though surface property is one tactile cue for stick/slip regulation, however, it is relatively difficult to quantify the surface property from the period values because the pulse period is normally within tens of millisecond. Within such fast slip period, the durations of stick-slip behavior among different interfacial properties vary insignificantly. Note that this phenomenon is also applicable to human fingertip because the manual scanning speed is normally located in the range, e.g., faster than 10 mm s^{-1}, that results in a fast stick-slip process (Figure 4e).

As indicated in previous reports, perceptions of surface roughness and scanning state are essential functions of human fingertip that cannot be separately considered.[26] During the scanning process, topology of the contact surface is another important parameter that is associated with the stick-slip phenomenon and cannot be excluded.[27] As depicted in Figure 6b, flat surface with smaller average roughness (Ra) allows the fingertip to ensure tight contact with the substrate during scanning. When the value of Ra is increased, the existence of air gap between the surface topology and human fingertip might reduce the contact between the fingertip and the target surface. Consequently, increase of Ra could result in tiny stretch of the skin and a stick-slip process cannot be supported (Figure 6c). Alternatively, full slip will be generated during the interaction process when fingertip scans across the rough surface. To confirm the effect from surface roughness, Figure S29 in the Supporting Information provides the details of roughness from the surfaces studied in Figure 6a. The results show that compared with other substrates, paper exhibits a relatively higher degree of roughness with Ra of 1.985 ± 0.0091 µm. We further applied rougher sandpaper substrate to study the impact from surface roughness. Regarding this, three different types of sandpaper with varying grit sizes (P400, P1500, and P2500) were introduced. Also, we duplicated the P400 sandpaper surface to a pure PDMS substrate for comparison. The optical images in Figure S30 in the Supporting Information shows the rough surface from four different samples, and the electrical signals confirm that full slip occurs when the flexible device scanned across all samples. Unlike pure PDMS with a smooth surface, the rough PDMS also could not support the stick-slip behavior when contacting with the flexible device. This illustrates that only sliding process appears during the sliding of flexible sensor on rough PDMS substrate. Enlarged view of the contact between the flexible device and different substrates was provided in Figure S31 in the Supporting Information. Tight contact without air gap was observed when the device was pressed toward the flat glass. In contrary, air gaps were clearly observed when the flexible device was pressed toward different sandpapers under the same normal load. To verify whether the contact tightness can be compensated with a larger load, we applied the device to scan across surfaces with varying softness and roughness, which were demolded from sandpapers by soft PDMS (Figure S32a, Supporting Information). The soft substrate allows the surfaces to contact each other once the normal load was increased. Compared with electrical signals produced on sandpaper (Figure S32b, Supporting Information), obvious peak was observed when the device scanned across PDMS surface (Figure S32c, Supporting Information). Such behavior might be attributed by the enhanced adhesion between the device surface and soft PDMS. However, stick-slip process is still absent even though normal load was increased and a tight contact between the device and PDMS surface is ensured (Figure S32d, Supporting Information). A more strategic approach is applied by changing the specific roughness of the acrylic substrate. We polished the flat acrylic sample via a commercial sandpaper, and the roughness degree was controlled based on different abrading cycles (Figure S33, Supporting Information). Up to 30 abrading cycles, the values of Ra continuously increase from 0.379 ± 0.0035 to 1.246 ± 0.0113 µm (Figure S34, Supporting Information). The optical images in Figure 6d further reveal the surface roughness is obviously increased from the original acrylic to the one after 30 cycles' manual wear. When the flexible device was scanning across the acrylic substrates with different Ra, the current profiles were recorded (Figure 6e). A relatively flat acrylic surface supports the stick-slip process with periodical current pulses. However, with more cycles' wear, the stick-slip behavior vanished and the periodical pulse signals were not recorded as summarized in Figure 6f, indicating that transition from stick-slip to full slip behavior is controllable from the aspect of roughness degrees. In one respect, this can be attributed from the reduced effective contact area between the device and the rough substrate. In addition, the difference between static and kinetic frictional forces might be weakened when surface roughness is increased.[28] The results further support the hypothesis that surface roughness plays an important role to affect the stick-slip process. From this perspective, the ridge-based device is also of significant potential to integrate with other tactile sensors that enriches the perceptive function of electronic skins.

Apart from irregular surface roughness, human can also obtain topological information by sliding the fingertip across a substrate with periodical patterns. As depicted in Figure 6g, the scanning of fingertip over patterns would result in obvious skin deformation and recover in normal direction, which allows the nervous system to quantitatively perceive the topology upon receiving related signals.[29] Induced by "stick-slip" process, lateral skin stretching caused by friction simultaneously provides alternative clue to reflect the behavior of stick/slip status. However, it is still challenging for conventional sensors to fully mimic such synchronous perception because of the inherent structural limitation to support both normal and lateral deformations. As mentioned above, the ridge-based assembly allows the flexible

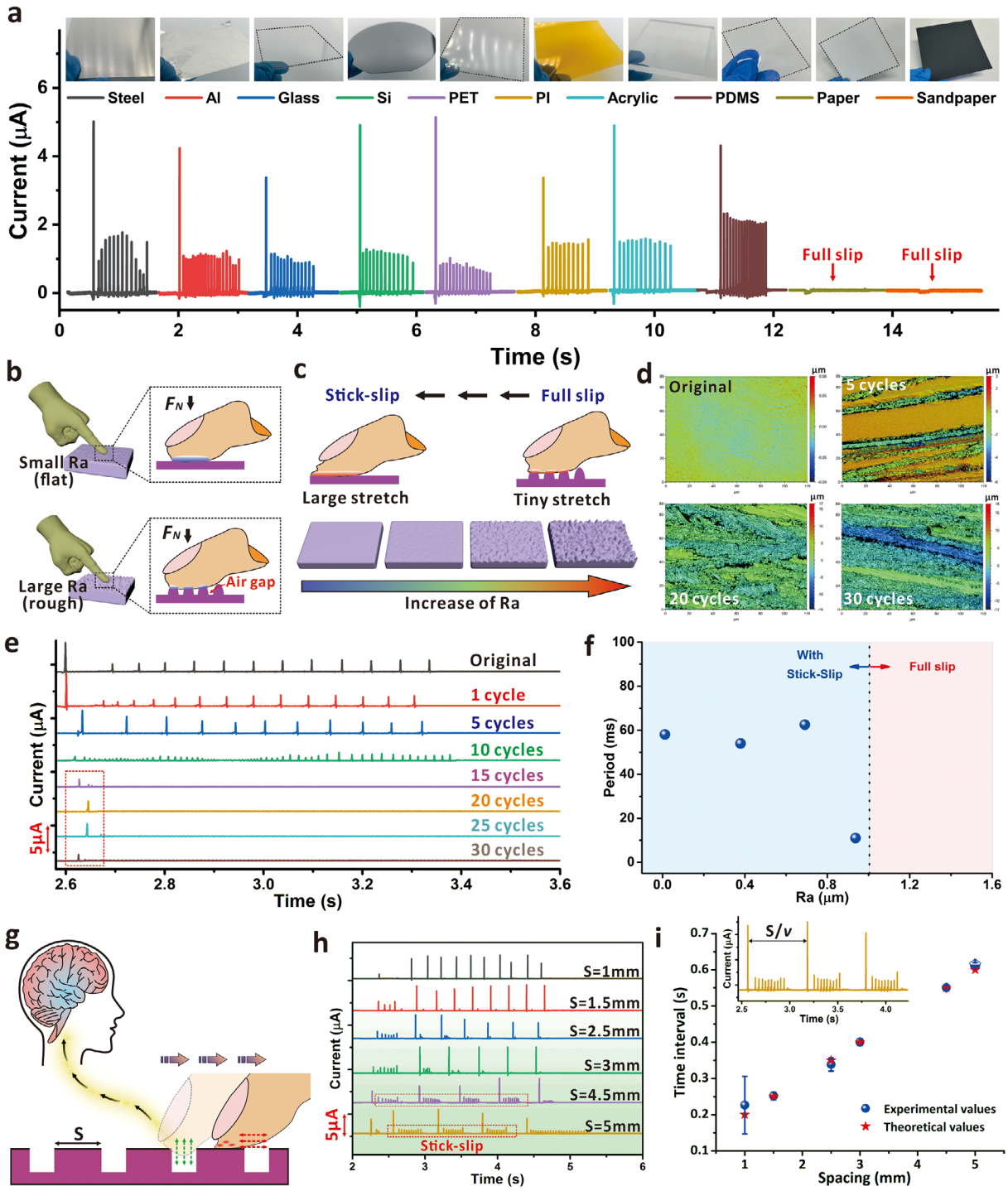

Figure 6. a) Current profiles when the flexible device scans across different surfaces, with the optical images of the substrates inserted. The scanning velocity and the normal force are 10 mm s^{-1} and 1.5 N, respectively. b) Diagram of the contact difference when human finger is approaching the surface with different roughness. c) Schematic diagram of fingertip scanning across surface with different roughness that renders different degrees of stretch. d) Optical images showing the surface roughness of acrylic substrates with different cycles' abrasive operation. The average surface roughness (Ra) is 0.012 ± 0.0006, 0.691 ± 0.0064, 1.167 ± 0.0282, and 1.480 ± 0.0197 μm for original sample, substrate abraded by 5 cycles, 20 cycles, and 30 cycles, respectively. e) Electrical profiles when the flexible device scans across acrylic substrates abraded by sandpaper with different cycles. f) Summary of the relationship between pulse period and the surface roughness of acrylic substrate. For cases of full slip, no period was recorded due to the absence of electrical pulses. g) Schematic diagram of signal transmission in nervous system when human fingertip scans across the surface patterns, where "S" represents the spacing between two adjacent concave stripes. h) Electrical profiles when flexible sensor was scanning across acrylic substrates with stripe patterns in different spacing values. i) Relationship between the time intervals of the main pulse and the pattern spacing. The theoretical and experimental values were plotted for comparison.

architecture to withstand perpendicular deformation with recover capability. Therefore, we designed the patterned acrylic samples with different spacing between two adjacent concave stripes (Figure S35, Supporting Information), to investigate the signal profiles when surface patterns were involved. In our case, we fixed the width of the concave stripe at 1 mm, while varying the convex spacing (S) from 1 to 5 mm. Figure S36 in the Supporting Information describes the full scanning process across the patterned acrylic substrate using the ridge-based flexible sensor. Initially, a typical stick-slip process occurs before the edge of the device reaching the first stripe pattern (Step 1). During this period, periodical pulses were observed with a relatively short period and low intensity behavior because of the limited stretching. When reaching the first convex stripe, the pattern imposes resistance to the device from moving forward, which produces a significant pulse once the device is released from such mechanical constraint (Steps 2 and 3). Subsequently, the continuous sliding will result in repeated stick-slip behavior to produce similar periodical impulse that is related with the periodical ridge stretching and recover (Step 4). From this view, it is reasonable that a larger convex spacing will favor the behavior of stick-slip because of sufficient direct contact area. On reaching subsequent stripes with larger spacing, stick-slip processes may occur due to increased allowable motion distance (large S). During the scanning process, intensified pulses were periodically produced for all spacing conditions from 1 mm to 5 mm (Figure 6h). Via measuring the time intervals between two adjacent intensified peaks, we compared the experimental values with the theoretical ones as provided in Figure 6i. In principle, theoretical time intervals can be obtained based on the ratio, S/v, between the spacing and the scanning speed (10 mm s^{-1}). The results exhibit excellent consistence, indicating that the significant peaks originate from the periodical patterns under investigation. Unlike the intensified pulses, stick-slip process cannot be observed from all investigated samples with different spacing. As emphasized in Figure S37 in the Supporting Information, nine intensified peaks were recorded with a relatively small spacing of 1 mm, which is originated from the stripe patterns and consistent with the layout in Figure S35 in the Supporting Information. However, the periodical pulses related with stick-slip process were only observed in the cases with larger spacing, e.g., 4.5 and 5 mm (as indicated in the blue rectangle). For instance, apart from the four intensified peaks (labeled ①-④) in the electrical profiles, numerous periodical peaks with lower intensity were generated. The results indicate that the successful generation of stick-slip behavior requires sufficient contact region between the flexible device and the target surface, which is different from the perception of topological information that mainly depends on the deformation in normal directions. Furthermore, a larger spacing also facilitates the stick-slip process because the topological interference can be potentially avoided. Video S6 in the Supporting Information also compares the difference when the device was scanning across the substrates with S of 1 and 5 mm. Typical ridge stretching and recovery were not observed in the case of $S = 1$ mm (Figure S38, Supporting Information), while stick-slip behavior was clearly found in the case of $S = 5$ mm. The results experimentally confirm that the status of full slip and stick-slip is related with the surface topologies, which is also consistent with the electrical signals in Figure 6h. Upon further signal decoding, it is of significant potential that the developed device is capable to provide more information of the target surface under study. As the pulse intensity is mainly associated with the fast slip process, it also can be expected that further enhancement of the periodical signals can be realized if more magnetized component, e.g., mass ratio of NdFeB particles, is introduced into the composite matrix. With further optimization, e.g., scaling-down of the device, we expect the study herein can also provide a comprehensive guidance to design wearable sensors that fully explore the function of human finger especially in perceptive duplication of the stick/slip status.

3. Conclusion

In this study, we introduced a unique magnetism-coupled approach to revisit the stick/slip states when human fingertip slides across a target surface. The designed sensor, with flexible and deformable ridge-type layer, is capable to endure lateral deformation with recover ability when tangential friction was applied. Using a customized setup, we experimentally analyzed the key factors that influence the "stick-slip" behavior during the scanning process. It was demonstrated that the intrinsic elastic strength of the ridge layer and the difference in static and kinetic frictions render a successful stick-slip process. Thanks to the built-in magnetized orientation, the mechanical deformation can be directly converted to periodical electrical pulses during the rapid slip state. Our results indicate that the pulse periods are dependent on sorts of factors including ridge geometry and inherent matrix modulus, and operational parameters such as scanning speed and normal load, where the relationships exhibit high consistency with the theoretical model and provides an effective clue to perceive surface information. More interestingly, we found that the transition from stick-slip to full slip is also influenced by factors such as surface moisture, roughness degree, and topological patterns. In addition, we show that the flexible device is attachable on human fingertip to mimic the distinct stick-slip or full slip process when crossing different surfaces. This study not only strengthens our understanding of the interaction when fingertip scans across a specific surface, but also sets the stage to explore more dimensional perceptions of wearable tactile sensors in future.

4. Experimental Section

Materials: Neodymium-iron-boron (NdFeB) powders were purchased from Magnequench Co., Ltd., China as the magnetized source. Two soft substrates, polydimethylsiloxane (PDMS) and Ecoflex 00-50, were obtained from Dow Corning, USA and Smooth-On, Inc., USA. Double-sided copper flexible conductive materials for coil fabrication were obtained from Chengdu d'Itc New Material Co., Ltd., China. Commercial SiC sandpapers with different grits (P400, P2000, and P2500) were purchased from Starcke GmbH and Co. KG, Germany. Polyimide film with thickness of 25 µm was obtained from Shanghai Zhong Bin Technology Co., Ltd., China. Soda-lime glass and polyethylene terephthalate (PET) substrates were purchased from Zhuhai Kaivo Optoelectronic Technology Co., Ltd., China.

Characterizations: Scanning electron microscopy and EDS mapping images were obtained by field-emission scanning electron microscopy (Carl Zeiss, Germany). The induced current pulses in stick-slip process were collected by low-noise current preamplifier (SR570, SRS, USA) and multifunctional I/O device (USB-6341, NI, USA). Periodical stick-slip movement of the designed devices was recorded by high-speed camera (VEO 1010L, Phantom, USA) at rate of 5000 fps (frames per second).

Scanning speed of the deformable device in standard characterization was controlled by motorized platform (MAR 100-90, Zolix Instruments, China). The initial normal load and the change of the load were measured by commercial force gauge (M5-20, Mark-10, USA). The roughness of the surface was measured by 3D Optical Profilometers (ContourGT-K, Bruker, Germany). The variation of the localized magnetic intensity was measured by three axis Gauss/Tesla Meter (DX-360, Dexin Mag, China). During the measurement, the gauss probe was placed horizontally on the central position above the top layer of the device. The device was fixed on the motorized platform, which was moving back-and-forth with a displacement of 10 mm under a defined velocity of 10 mm s^{-1}. With the movement, the device will deform/recover accordingly and corresponding magnetic field variation at the representative position was recorded by the gauss probe in real-time. For the wearable demonstrations, informed consents were obtained from the volunteers before the tests. According to the relevant regional regulations, the involved characterizations are in vitro, nonclinical, and nontoxic. No formal approval from institutional authorities was required.

Fabrication of Deformable Sandwich-Like Structure: A plastic mold engraved with the ridge shape of the middle layer, and a bottom layer with dimension of 1 cm × 1 cm × 0.8 cm (length × width × depth) was prepared. A mixture of NdFeB microparticles, PDMS, and Ecoflex in a specific mass ratio was then poured into the mold. The filled mold was placed in a vacuum chamber for degassing at room temperature to remove the trapped air bubble, and was subsequently placed horizontally in an oven to solidify at 80 °C for another 30 min. The resulting integrated structure of the middle and bottom layers was then removed from the mold. Pure PDMS gel was then filled into another mold containing the same shape as that of the bottom layer to form the top layer, followed by the same degassing and curing procedures as described above. Subsequently, a small amount of unsolidified PDMS substrate was evenly coated on the prepared transparent top layer, and the integrated structure was aligned in parallel and placed onto the pure PDMS layer. After complete curing at 80 °C for 30 min, the coating layer can bond the top layer and the integrated structure tightly to form a stable sandwich-like structure with resistance to shear deformation. Finally, by subjecting this prepared structure to an external magnetic field strength of ≈3 T in a specific orientation, the desired magnetized flexible device was obtained for "stick-slip" investigation.

Fabrication of Flexible Coil: The double layer copper coil was obtained by engraving the substrate through ProtoLaser machine (U4, LPKF, Germany). The substrate with total thickness of 111 µm contains three layers and insulating polyimide layer was used to separate two copper layers with thickness of 18 µm. Silver paste was used to fill a through hole with a diameter of 1.2 mm in the center of the coils to connect the two conductive layers. There were ≈25 loops in each coil layer, and the width for each loop and gap width between two adjacent loops were 80 µm. The electrical resistance for the whole coil was about 16.5 Ω.

Signal Collection and Analysis: The conductive coil transmits the induced current to a low-noise current preamplifier, and these signals will be output in real time to the LabVIEW interface via DAQmx series subVIs. The sample rate and filter frequency were set at 10 000 times s^{-1} and 1 kHz, respectively. Subsequently, automatic peak detection in the data analysis module of OriginLab software was utilized to extract the coordinates of the current pulses. Due to the rapid completion of the sliding process, the time difference between two adjacent peaks is approximated as the time interval between two sliding processes. The average time interval from the third to eighth groups is considered as representative period of the stick-slip process. This is to exclude the potential influence from the acceleration and deceleration moments of the motorized platform during the characterization.

Acquirement of Shear Modulus: NdFeB microparticles, PDMS, and Ecoflex mixture with varying mass ratios were initially poured into molds containing stripe shapes (3 cm × 1 cm × 0.1 cm) respectively. After degassing and heating at 80 °C for 20 min, stripes of uniform size but different elasticities were obtained. Subsequently, the two ends of these stripes were affixed to the motion fixture. The force gauge recorded real-time tensile forces at different degrees of tension, while a microscope captured images depicting the states of different materials before and after stretching. The percentage of strain in length was linearly fitted to the average pressure in the cross-sectional area, and the slope of the fitted line was applied to represent the elastic modulus (E) of each material. Additionally, the changes in length and width, before and after stretching, were measured to obtain the value of Poisson ratio (σ) for the matrix prepared in different mass ratios. Finally, the shear modulus (G) of the matrix in different mass ratios was calculated based on the governing formula $G = \frac{E}{2(1+\sigma)}$.

Simulation of Mechanical Performance: The 3D models of the flexible sensor were established in COMSOL Multiphysics 5.6 software for mechanical performance analysis. The geometric parameters of each model are the same as those used in the experiments. The elastic material applied to the flexible device is default PDMS in software. Based on solid mechanics module, the governing equation that was used to the analysis the internal stress and deformation was $0 = \nabla \cdot (SF)^T + F_v$, where F_v is the volumetric force, F is deformation gradient and S is the second Piola-Kirchhoff stress tensor. The top layer of the device in the simulation model was fixed and applied with 1 N boundary load in normal direction. The bottom layer was applied with 0.38 N in horizontal direction to mimic the frictional force as an example. The reason to use 0.38 N as frictional force is that the dynamic frictional force was approximated as the maximum static value. The force was calculated by the basic formula ($f = \mu N$) and the value for coefficient of friction between glass and PDMS is 0.38 in the simulation model.[30] Finally, force distribution of the flexible device in steady condition among the device matrix was obtained for analysis. For the deformation related with different ridge heights, similar simulation model was applied to evaluate the lateral displacement.

Statistical Analysis: In this work, the data were expressed as the "mean ± standard deviation". Error bars in all figures for average periods are the standard deviations obtained from five individual periods unless otherwise stated. For the surface roughness, the average values were obtained from at least three independent measurements on the same substrate. All data were analyzed and performed by Origin Software.

Supporting Information

Supporting Information is available from the Wiley Online Library or from the author.

Acknowledgements

This work was supported by The Science and Technology Development Fund, Macau SAR (File No. FDCT-0057/2023/RIB2), Guangdong Science and Technology Department (2022A0505030024), and University of Macau (MYRG-GRG2024-00090-IAPME). The author contribution is as follows: formal analysis, methodology, and writing original paper (D.F.); circuit design and experimental methodology (S.D.); investigation and experimental methodology (Y.L.); discussion and visualization (Q.Z.); discussion and analysis (B.Q.); discussion and visualization (B.J.); funding acquisition, conceptualization, review, and editing paper (B.Z.).

Conflict of Interest

The authors declare no conflict of interest.

Data Availability Statement

The data that support the findings of this study are available from the corresponding author upon reasonable request.

Keywords

flexible sensors, magnetized devices, slip phase, stick-slip, tactile perceptions

Received: November 18, 2024
Revised: February 17, 2025
Published online: March 19, 2025

[1] G. Corniani, H. P. Saal, *J. Neurophysiol.* **2020**, *124*, 1229.
[2] R. S. Johansson, J. R. Flanagan, *Nat. Rev. Neurosci.* **2009**, *10*, 345.
[3] a) L. Shi, Z. Li, M. Chen, T. Zhu, L. Wu, *Adv. Mater.* **2023**, *35*, 2210091; b) H. Gu, B. Lu, Z. Gao, S. Wu, L. Zhang, L. Xie, J. Yi, Y. Liu, B. Nie, Z. Wen, X. Sun, *Adv. Funct. Mater.* **2024**, *34*, 2410661; c) Y. Gao, B. Zhang, Y. Liu, K. Yao, X. Huang, J. Li, T. H. Wong, Y. Huang, J. Li, J. Zhou, M. Wu, H. Li, Z. Gao, W. Park, C. K. Yiu, H. Jia, R. Shi, D. Li, X. Yu, *Adv. Mater. Technol.* **2022**, *8*, 2200759; d) Y. Liu, J. Tao, Y. Mo, R. Bao, C. Pan, *Adv. Mater.* **2024**, *36*, 2313857.
[4] a) X. Guo, Z. Sun, Y. Zhu, C. Lee, *Adv. Mater.* **2024**, *36*, 2406778; b) D. Filingeri, D. Fournet, S. Hodder, G. Havenith, *J. Neurophysiol.* **2014**, *112*, 1457.
[5] B. P. Delhaye, F. Schiltz, A. Barrea, J. L. Thonnard, P. Lefevre, *J. Neurophysiol.* **2021**, *126*, 1455.
[6] A. M. Smith, G. Basile, J. Theriault-Groom, P. Fortier-Poisson, G. Campion, V. Hayward, *Exp. Brain Res.* **2010**, *202*, 33.
[7] a) Z. Sun, M. Zhu, X. Shan, C. Lee, *Nat. Commun.* **2022**, *13*, 5224; b) S. Z. Liu, W. T. Guo, H. Chen, Z. X. Yin, X. G. Tang, Q. J. Sun, *Small* **2024**, *20*, 2405520; c) Y. Jiang, L. Fan, H. Wang, Z. Luo, W. Zhang, J. Wang, X. Sun, N. Li, J. Tian, *Nano Energy* **2024**, *131*, 110279.
[8] a) C. Lv, C. Tian, J. Jiang, Y. Dang, Y. Liu, X. Duan, Q. Li, X. Chen, M. Xie, *Adv. Sci.* **2023**, *10*, 2206807; b) M. Kundu, D. Mondal, N. Bose, R. Basu, S. Das, *ACS Appl. Nano Mater.* **2024**, *7*, 1804.
[9] a) Y. Wang, J. Chen, D. Mei, *Micromachines* **2019**, *10*, 579; b) Q. He, Z. Feng, X. Wang, Y. Wu, J. Yang, *ACS Appl. Mater. Interfaces* **2022**, *14*, 49295.
[10] D. Fang, S. Ding, Q. Zhou, D. Zhao, J. Zhong, B. Zhou, *ACS Nano* **2024**, *18*, 1157.
[11] J. Man, Z. Jin, J. Chen, *Adv. Sci.* **2024**, *11*, 2306832.
[12] Y. Li, M. Zhao, Y. Yan, L. He, Y. Wang, Z. Xiong, S. Wang, Y. Bai, F. Sun, Q. Lu, Y. Wang, T. Li, T. Zhang, *Npj Flexible Electron.* **2022**, *6*, 46.
[13] A. D. Berman, W. A. Ducker, J. N. Israelachvili, *Langmuir* **1996**, *12*, 4559.
[14] D. Babu, M. Konyo, H. Nagano, S. Tadokoro, *IEEE Trans. Haptics* **2018**, *11*, 417.
[15] J. Monnoyer, L. Willemet, M. Wiertlewski, *J. R. Soc. Interface* **2023**, *20*, 20220718.
[16] T. Putelat, J. H. P. Dawes, *J. Mech. Phys. Solids* **2015**, *78*, 70.
[17] B. T. Gleeson, S. K. Horschel, W. R. Provancher, *IEEE Trans. Haptics* **2010**, *3*, 177.
[18] a) C. Schwarz, *Trends Neurosci.* **2016**, *39*, 449; b) C. J. Miller, C. A. Zorman, G. E. Wnek, *Sens. Actuators, A* **2020**, *303*, 111824.
[19] E. Amaied, R. Vargiolu, J. M. Bergheau, H. Zahouani, *Wear* **2015**, *332–333*, 715.
[20] Z. Feng, Q. He, X. Wang, Y. Lin, J. Qiu, Y. Wu, J. Yang, *ACS Appl. Mater. Interfaces* **2023**, *15*, 6217.
[21] S. Derler, G. M. Rotaru, *Wear* **2013**, *301*, 324.
[22] M. J. Adams, B. J. Briscoe, S. A. Johnson, *Tribol. Lett.* **2007**, *26*, 239.
[23] M. Tomimoto, *J. Bionic Eng.* **2014**, *11*, 98.
[24] N. Tomita, S. Tamai, E. Okajima, Y. Hirao, K. Ikeuchi, Y. Ikada, *J. Appl. Biomed.* **1994**, *5*, 175.
[25] X. Zhou, J. L. Mo, Y. Y. Li, Z. Y. Xiang, D. Yang, M. A. Masen, Z. M. Jin, *Tribol. Lett.* **2020**, *68*, 85.
[26] S. Okamoto, H. Nagano, Y. Yamada, *IEEE Trans. Haptics* **2013**, *6*, 81.
[27] Y. Lu, D. Han, Q. Fu, X. Lu, Y. Zhang, Z. Wei, Y. Chen, *Tribol. Int.* **2025**, *201*, 110221.
[28] Y. Kligerman, M. Varenberg, *Tribol. Lett.* **2013**, *53*, 395.
[29] T. Hamasaki, M. Iwamoto, *Adv. Mech. Eng.* **2019**, *11*, 1.
[30] E. H. Bani-Hani, J. Lopez, G. Mohanan, *Data Brief* **2019**, *22*, 940.